JGR Space Physics

RESEARCH ARTICLE
10.1029/2018JA025988

The 3-D Distribution of Artificial Aurora Induced by HF Radio Waves in the Ionosphere

A. Kvammen[1], B. Gustavsson[1], T. Sergienko[2], U. Brändström[2], M. Rietveld[1,3], T. Rexer[1], and J. Vierinen[1]

[1]Department of Physics and Technology, University of Tromsø-The Arctic University of Norway, Tromsø, Norway, [2] Swedish Institute of Space Physics, Kiruna, Sweden, [3]EISCAT Scientific Association, Ramfjordbotn, Norway

Key Points:
- The first 3-D estimates of induced emission at 8,446 Å are presented along with 3-D estimates of the enhanced emission at 6,300 and at 5,577 Å
- The altitude distribution of the resulting excitation rates is inconsistent with excitation rate predictions
- We observe that the emission enhancements are strongly dependent on the pump frequency proximity to the double resonance

Correspondence to:
A. Kvammen,
andreas.kvammen@uit.no

Citation:
Kvammen, A., Gustavsson, B., Sergienko, T., Brändström, U., Rietveld, M., Rexer, T., & Vierinen, J. (2019). The 3-D distribution of artificial aurora induced by HF radio waves in the ionosphere. *Journal of Geophysical Research: Space Physics*, *124*, 2992–3006. https://doi.org/10.1029/2018JA025988

Received 10 AUG 2018
Accepted 12 MAR 2019
Accepted article online 21 MAR 2019
Published online 6 APR 2019

Abstract We present 3-D excitation rate estimates of artificial aurora in the ionospheric *F* layer, induced by high-frequency radio waves from the European Incoherent Scatter heating facility. Simultaneous imaging of the artificial aurora was done with four separate Auroral Large Imaging System stations, permitting tomography-like 3-D auroral reconstruction of the enhanced atomic oxygen emissions at 6,300, 5,577, and 8,446 Å. Inspection of the 3-D reconstructions suggests that the distribution of energized electrons is less extended in altitude than predicted by transport calculations of electrons accelerated to 2–100 eV. A possible reason for this discrepancy is that high-frequency pumping might induce an anisotropic distribution of energized electrons.

Plain Language Summary Auroral lights can be artificially generated by transmitting high-frequency radio waves with high power into the upper atmosphere. In this article, we use multiple viewpoint imaging of artificially produced aurora to estimate the 3-D distribution of the auroral lights by employing tomography-like techniques. The 3-D distribution is estimated in the red, green, and infrared auroral emission lines with wavelengths of 630.0, 557.7, and 844.6 nm, respectively. These emissions are excited by energetic electrons, which have been accelerated through interaction processes between the transmitted radio waves and plasma in the upper atmosphere, at an altitude of about 220–250 km. We observe that the estimated 3-D auroral distributions are less extended in altitude than indicated by previous theoretical work. A possible reason for this disagreement is that the radio wave-plasma interaction processes might lead to a direction dependent electron acceleration.

1. Introduction

When powerful high-frequency (HF) radio waves reach the ionosphere, several wave-plasma interactions are excited and most of the HF wave energy is dissipated by the plasma (Senior et al., 2012), inducing observable phenomena, such as electron temperature enhancements (Honary et al., 1995; Rietveld et al., 2003; Robinson, 1989), production of electron density striations (Milikh et al., 2008), artificial ionization (Bernhardt et al., 2016; Pedersen et al., 2009), stimulated electromagnetic emissions (Leyser, 2001), and enhancement of optical emissions (Brändström et al., 1999; Gustavsson et al., 2005). At auroral latitudes, it is postulated that incident ordinary mode HF radio waves excite upper-hybrid (Kosch et al., 2002), lower-hybrid (Djuth et al., 2005), and Langmuir turbulences (Djuth et al., 2004) as well as electron Bernstein waves (Stubbe et al., 1994) within magnetic field-aligned plasma striations in the ionosphere. The strong wave-plasma interaction region will have an upper border at the reflection altitude and a rough lower border at the altitude where the pump frequency is in resonance with the upper-hybrid frequency (Eliasson & Papadopoulos, 2015), typically a few kilometers below the reflection altitude for *F* region heating (Gustavsson et al., 2005).

The net result of these plasma processes is energization of electrons and increased plasma pressure within plasma striations (Gurevich & Zybin, 2006). This triggers an instability, known as the resonance instability (Gurevich, 2007), where the striations continue to expand as the plasma pressure increases, which causes self-focusing and increased HF radiation flux into the striations (Eliasson & Papadopoulos, 2015; Istomin & Leyser, 2003; Gondarenko et al., 2005). The striations will expand from a few meters to hundreds of meters during the first 10–30 s after heating onset before stabilizing, the expansion is primarily in the plane perpendicular to the magnetic field (Coster et al., 1985; Milikh et al., 2008). After that point, close to 100% of the

HF wave energy is dissipated by the plasma within the interaction region, provided that the pump power flux exceeds 30 μW/m^2 (Senior et al., 2012).

Observations of both enhanced plasma lines (Carlson et al., 1982) and enhanced optical emissions (Brändström et al., 1999) during heating can only be explained by high-energy electrons. Understanding how the electron energy distribution is modified during HF pumping is one of the central questions in ionospheric heating research. Mantas (1994) and Mantas and Carlson (1996) attempted to explain observations of enhanced emission intensities at 6,300 Å, denoted I_{6300}, during HF heating by $O(^1D)$ excitation (threshold 1.96 eV) from a purely thermal electron energy distribution. However, a thermal electron energy distribution cannot explain observations of enhanced emissions from states with higher excitation energies, such as I_{5577} from $O(^1S)$ (threshold 4.17 eV; Haslett & Megill, 1974), I_{8446} from $O(3p^3P)$ (threshold 10.99 eV; Gustavsson et al., 2005), and I_{4278} from $N_2^+(1NG)$ (threshold 18.75 eV; Holma et al., 2006). There are not enough high-energy electrons in a thermal population to induce observable enhancements at these wavelengths (Gustavsson et al., 2002). The observations are therefore in line with an accelerated, suprathermal, electron energy distribution (Bernhardt et al., 1989).

Gustavsson et al. (2005) and Gustavsson and Eliasson (2008) combined optical images of I_{6300}, I_{5577}, I_{8446}, and I_{4278} and IS radar observations to estimate the energy and altitude distribution of electrons accelerated to 2–100 eV during heating. Gustavsson and Eliasson (2008) achieved this by employing a two-stream electron transport model with isotropic electron acceleration by upper- and lower-hybrid waves within a narrow altitude range, taking electron-ion and electron-neutral collisions into account. Hysell et al. (2012) and Hysell et al. (2014) obtained similar results of the suprathermal electron energy distribution versus energy and altitude using spectrographic measurements and electron transport from the multistream SAMI2-PE model (Varney et al., 2012). These results provide a method for calculating the altitude distribution of HF-enhanced optical emissions by employing the appropriate excitation cross sections and transition probabilities. So far, there have been no attempts at comparing the resulting electron energy distributions and the corresponding excitation rates to volumetric emission rate estimates. The 3-D emission rate estimates of heating induced I_{6300} were for the first time estimated by Gustavsson et al. (2001) using the European Incoherent Scatter (EISCAT) heating facility and simultaneous multistation imaging at three Auroral Large Imaging System (ALIS) imaging stations. Gustavsson et al. (2001) achieved 3-D emission rate reconstruction by using tomography-like inversion methods. The same method was later employed by Gustavsson et al. (2008) to estimate the volume emission rates in both I_{6300} and in I_{5577} using the High-Frequency Active Auroral Research Program facility and two imaging stations. Shindin et al. (2018) estimated the 3-D emission rates of I_{6300} at midlatitudes, induced by the Sura heating facility, using two imaging stations.

In this paper, we use multistation optical observations of I_{6300}, I_{5577}, and I_{8446} to test predicted excitation-altitude profiles, calculated using the method described in Gustavsson and Eliasson (2008). This is achieved by comparing the projections of reconstructed 3-D aurora models to simultaneous multistation images. The first results of 3-D artificial auroral reconstruction from as many as four imaging stations in I_{6300} and in I_{5577} are presented along with the first published estimates of the I_{8446} volume distribution.

2. Experiment and Observations

The EISCAT Scientific Association heating facility (Rietveld et al., 2016), the EISCAT ultrahigh frequency (UHF) incoherent scatter radar (Rishbeth & Van Eyken, 1993), and ALIS (Brändström, 2003) were operating simultaneously on 16 February 2015. Heating array 3 was employed to transmit right-hand circular polarized HF waves, that is, ordinary mode waves in the ionospheric plasma, antiparallel to the magnetic field. A frequency of 6.200 MHz was used from 16:00 to 16:50 UT, that is, heating not close to a gyroharmonic resonance, and a frequency of 5.423 MHz from 16:51 UT and onward, that is, heating in proximity to the fourth gyroharmonic frequency. The HF pumping was operating in a 150-s heating on and 85-s heating off cycle modulation, making it possible to measure the sky background between the heating pulses and to estimate the decay time of the 6,300-Å emission. The growth and decay of the enhanced intensities in the 6,300-Å emission line, I_{6300}, are shown in Figure 1 for one heating cycle. The growth and decay time of I_{6300} are dependent on the effective $O(^1D)$ lifetime. The observed $O(^1D)$ lifetimes are presented in Figure 5 and are more thoroughly discussed in section 3.

The frequency-dependent effective radiated power was approximately 138.2 MW at 6.200 MHz and 115.9 MW at 5.423 MHz, corresponding to effective power fluxes of 143 and 120 μW/m^2 at the heating altitude (Rietveld et al., 1993). The modeled beam patterns are shown in Figure 2.

The EISCAT UHF incoherent scatter radar was operated with a meridional scan pattern throughout the experiment, providing plasma parameter measurements of the heated volume with approximately 3-km altitude resolution and 5-s time resolution. The electron temperature was enhanced to approximately 3300 K at the resonance height during 6.200-MHz heating and to about 2500 K when pumping at 5.423 MHz. The electron density and ion drift velocity remained stable throughout the time interval of interest, that is, no natural auroral activity and no ion upflow. The Beata pulse-coding scheme was employed, and plasma parameters were extracted from the backscattered power spectrum using the Guisdap analysis tool (Lehtinen & Huuskonen, 1996), version 8.8.

Optical imaging of the artificial aurora was made with ALIS in the emission lines at 6,300, 5,577, 8,446, and 4,278 Å; however, significant enhancements were only observed in 6,300, 5,577, and 8446 Å. The UHF electron temperature measurements and the enhanced emission intensities are presented in Figure 3. The electron temperature panel clearly shows a decrease in the pump enhanced temperatures when going from 6.200- to 5.423-MHz pumping, that is, from heating away from a gyroharmonic to heating near the fourth gyroharmonic. The scatter points in the optical intensity plots represent the mean intensity of a (11 × 11) pixel grid around the peak enhancement in the images. I_{6300} was strongest during 6.200-MHz heating; the enhancement was reduced by a factor 3 when changing pump frequency to 5.423 MHz. I_{5577} remained quite similar at 6.200- and at 5.423-MHz pumping, whereas significant I_{8446}, above a noisy background, was only detected during 5.423-MHz heating. Imaging was done at four ALIS stations, in Abisko, Kiruna, Silkimuotka, and Tjautjas. An exposure time of 6 s was chosen at all stations and for all filters, providing images approximately every 10 s. Clouds before 16.37 UT and clouds and interference after 17.00 obstructed optical observations. Tomographic reconstruction was therefore done between 16.37 and 17.00 UT. No images were taken in the 8,446-Å filter at Kiruna; hence, tomographic reconstruction of I_{8446} was done using only three imaging stations. In addition, note that the periodic electron temperature modulation, seen in the top panel of Figure 3 during heating on, is due to the scanning of the UHF radar beam through the heated volume. The UHF radar scanned over positions between 7.8°S and 15.5°S of zenith. The electron temperature enhancement peaked when the UHF beam was antiparallel to the magnetic field, although there is an asymmetry in the temperature enhancement between the bottom and the top of the meridional scan. It is not clear if there is a physical reason for the asymmetry or if it is solely a geometric effect.

The optical data acquired on 16 February 2015 were particularly suitable for 3-D reconstruction of artificial aurora for two reasons: (1) Enhanced emissions were observed from as many as four separate imaging stations, making the tomography-like inversion more reliable than in previous reconstruction attempts. (2) The artificial aurora was observed to have a simple continuous shape at all imaging stations and in all emission lines; see, for example, the 6,300-Å emission in Abisko in Figure 1. This enabled us to approximate the emission distribution by using simple Gaussian distribution functions. In contrast, a more structured artificial aurora with many small-scale striations, as seen during some High-Frequency Active Auroral Research Program experiments (e.g., Bernhardt et al., 2016; Kendall et al., 2010), or a drifting emission pattern, as seen by, for example, Grach et al. (2017), would cause the reconstruction problem to be much more complex and ambiguous.

3. Aurora Modeling

The 3-D artificial aurora reconstruction was achieved by adjusting a 3-D parameterized aurora model so that the model projections fitted the observed images. The 3-D aurora models were constructed with a two-dimensional Gaussian in the horizontal plane combined with three different profiles along the magnetic field: (1) Gaussian distribution, (2) Gustavsson-Eliasson profiles, and (3) modified Gustavsson-Eliasson profiles. The 3-D Gaussian distribution gave us an empirical model with search parameters for the peak excitation rate, I_0, the center coordinates, (x_0, y_0, z_0), and the horizontal and vertical widths (σ_{xy}, σ_z), in total of six model parameters. The Gustavsson-Eliasson profiles model, denoted the G-E model, and the modified Gustavsson-Eliasson profiles model, denoted the modified G-E model, used excitation rate profiles, calculated for a range of electron acceleration altitudes by employing the method described in Gustavsson and Eliasson (2008). This gave us a set of five model parameters: I_0, x_0, y_0, z_0, and σ_{xy}, for the physical G-E

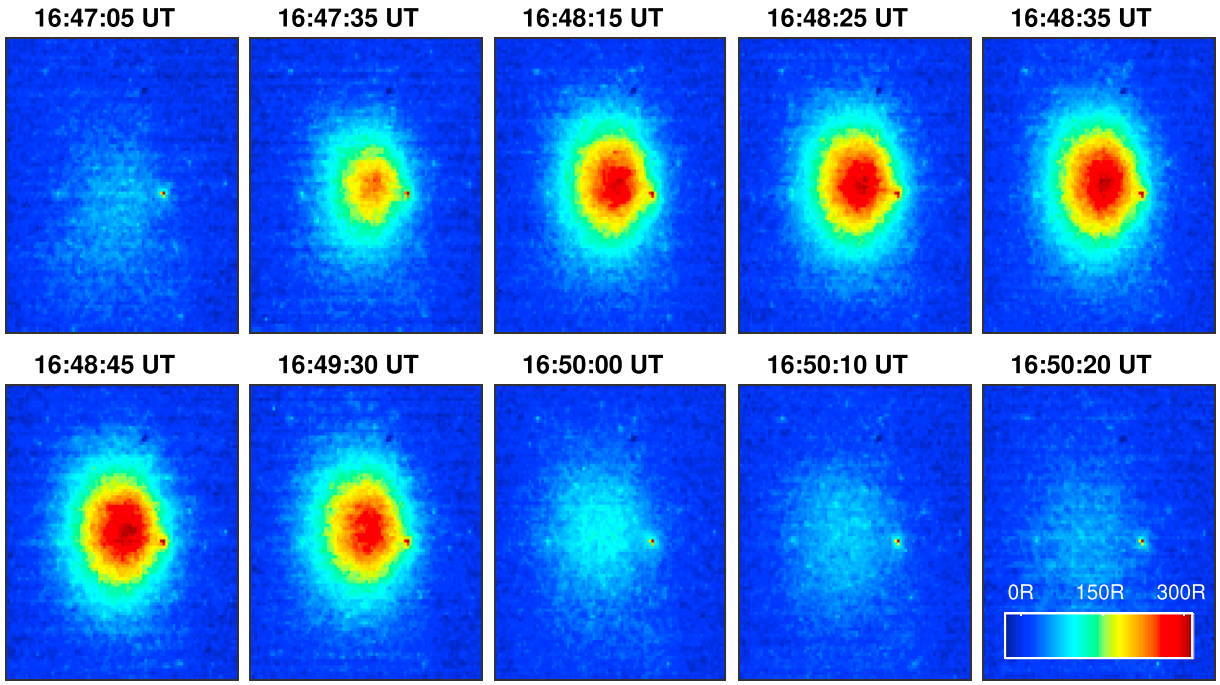

Figure 1. Images of the 6,300-Å emission in Rayleigh units [*R*] from one heating cycle as observed in Abisko. Images during heating are shown in the top row, and images after heating offset are in the bottom row. Note that the images are background reduced and flat field corrected, and the bright speckles are stars.

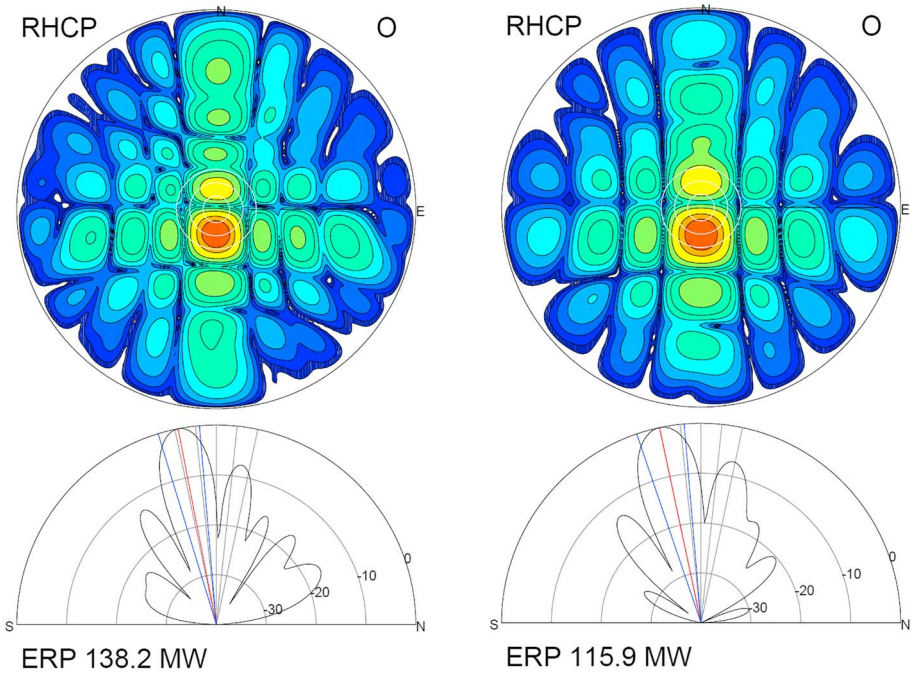

Figure 2. The figure shows the modeled beam patterns during 6.200-MHz heating to the left and during 5.423-MHz heating to the right. At the top, the 2-D radiation pattern where the white rings encircle zenith. At the bottom, the beam pattern in the meridional plane. The heating beam was pointed 12°S of zenith, approximately antiparallel to the magnetic field. RHCP = right-hand circular polarized; ERP = effective radiated power; O = ordinary mode.

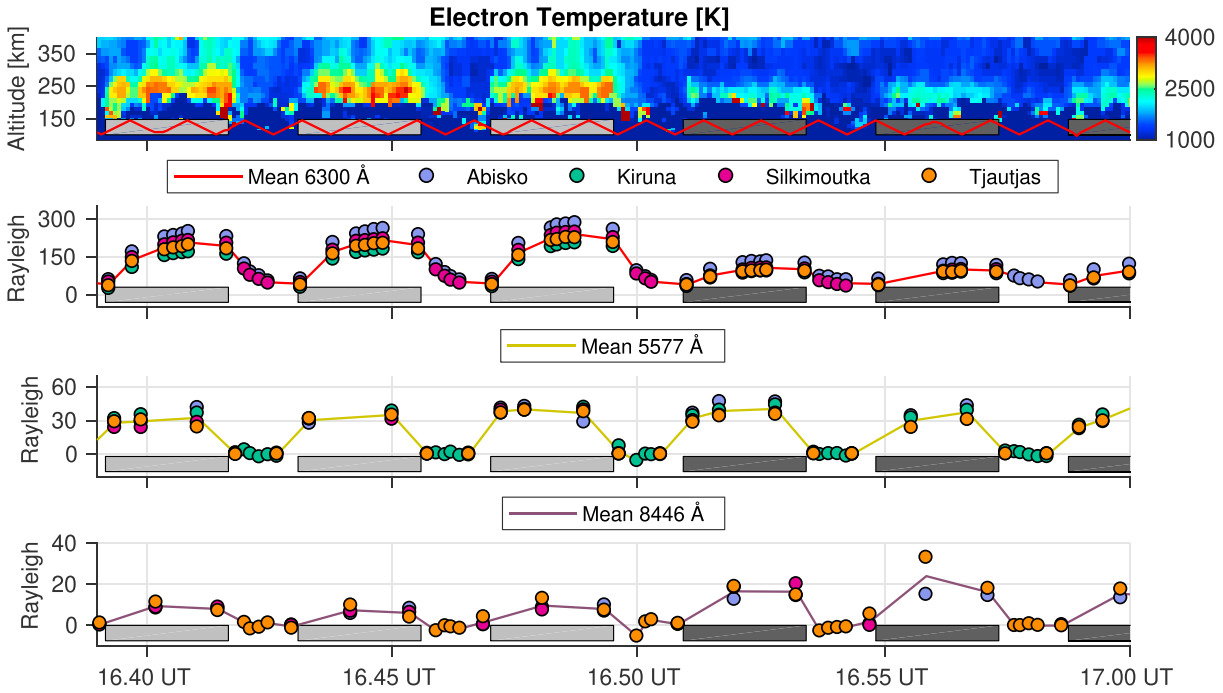

Figure 3. The European Incoherent Scatter ultrahigh frequency electron temperature observations and the enhanced emission intensities. The light gray boxes represent heating on during 6.200-MHz pumping and the dark gray boxes heating on at 5.423-MHz pumping. I_{6300} is not synchronized to the pump periods due to the long $O(^1D)$ lifetime. The scanning of the ultrahigh frequency radar beam through the heated volume is represented by the red line in the electron temperature panel.

model. An additional fitting parameter, γ, was used for adjusting the excitation rate profiles in the modified G-E model. Thus, six model parameters were used in the modified G-E model; $I_0, x_0, y_0, z_0, \sigma_{xy}$, and γ. Notice that the modified G-E model can be considered as a hybrid model, using the excitation rate profiles as the physical G-E model but is allowed for adjustment using the empirical γ parameter. The volume excitation rate model functions and the corresponding fitting parameters are described in more detail in Appendix A. It should be noted that increasing the number of fitting parameters, for example, allowing the excitation rates to be asymmetrical in the horizontal plane and adding more shape parameters along the magnetic field, would improve the fit to the observed data. However, we aimed at parameter fitting of unambiguous 3-D models with low parameter correlation and therefore employed few 3-D modeling parameters.

3.1. Parameter Fitting

A regularized version of the least squares error function, equation (1), was used in an iterative fitting process to determine the best fit 3-D aurora model parameters. The best fit parameters constructed 3-D emission models, which minimized the difference between the observed and the modeled images. The model images were produced by projecting the 3-D emission distribution down to the location of the imaging stations. An example of a best fit 3-D aurora model is presented in Figure 4 along with the comparison of the observed and modeled images for each of the four imaging stations: Abisko, Kiruna, Silkimuotka, and Tjautjas. The coordinates of the image station in Kiruna was chosen as origin. The coordinates of the 3-D model in Figure 4 are therefore given with respect to the Kiruna imaging station. The dot-projection algorithm, described in Rydesäter and Gustavsson (2000), was employed to calculate the projections of the 3-D aurora models. Several start guesses were used in the fitting process to avoid parameter searching in local minima. The model parameters at each iteration step was determined by the Nelder-Mead simplex search algorithm (Lagarias et al., 1998).

$$E(\mathbf{V}_t) = \arg\min_{\mathbf{V}_t}\left(\frac{1}{N_s}\left(\sum_s\sum_{i,j}[p_s(i,j) - \tilde{p}_s(i,j,I(\mathbf{V}_t))]^2 + W\sum_s|\mathbf{m_s} - \tilde{\mathbf{m}}_\mathbf{s}|^2\right)\right) \quad (1)$$

$E(\mathbf{V}_t)$ is the error function of the fitted parameter vector $\mathbf{V}_t$ at time t. N_s is the number of imaging stations, s is the station index, and (i,j) is the pixel index. $p_s(i,j)$ is the observed image in station s after

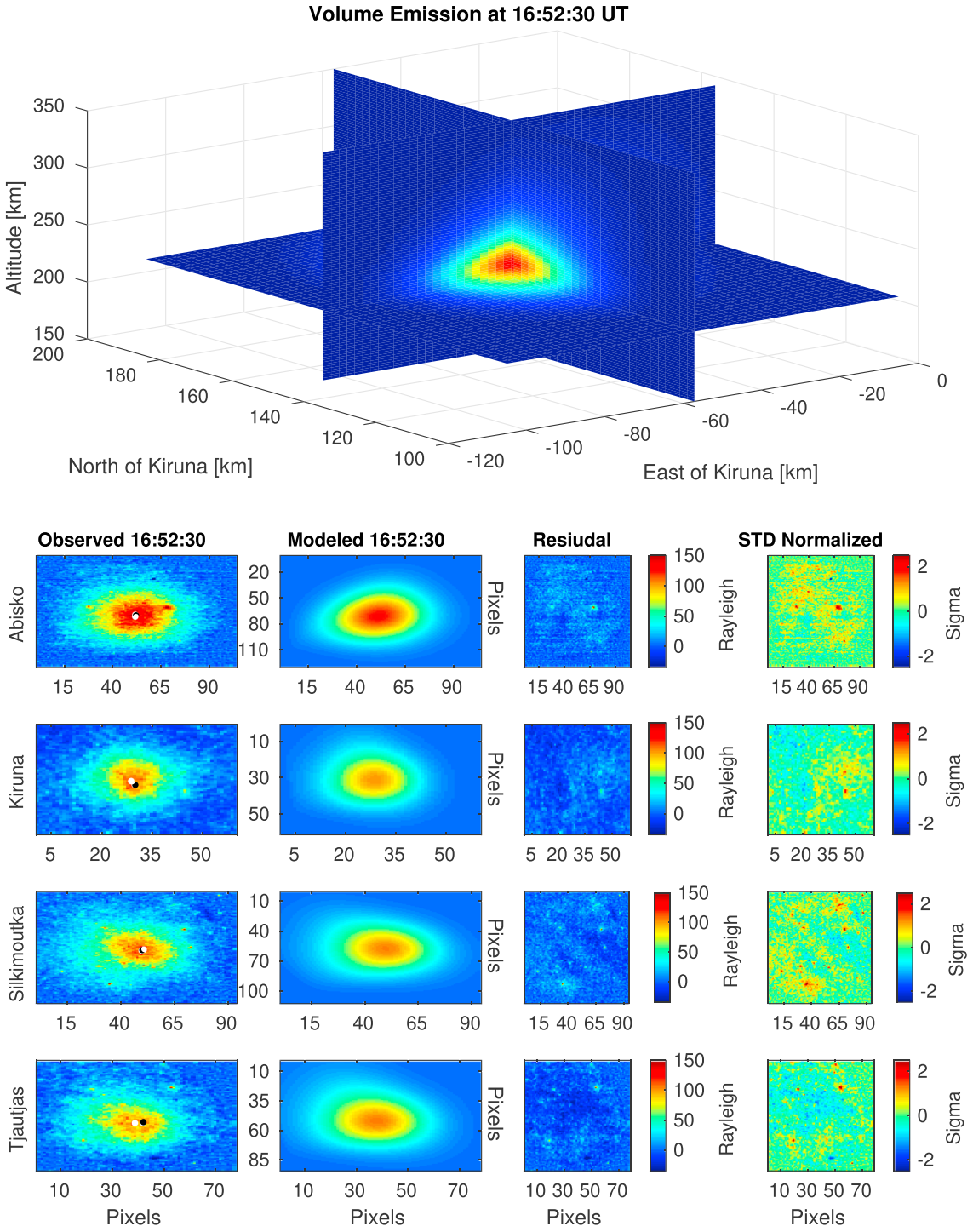

Figure 4. At the top, the best fit 3-D model of the 6,300-Å emission distribution at 16.52.30 UT. The 3-D distribution was constructed with the modified G-E model. At the bottom, the comparison between the observed and the modeled images. The first column shows the observed images for each of the four Auroral Large Imaging System stations. The second column shows the matching projections of the 3-D model. The third column shows the residual, that is, the pixel values in the observed images subtracted from the pixel values in the modeled images. The fourth column also shows the residual, but with the pixel values normalized with the standard deviation (STD) of the observations.

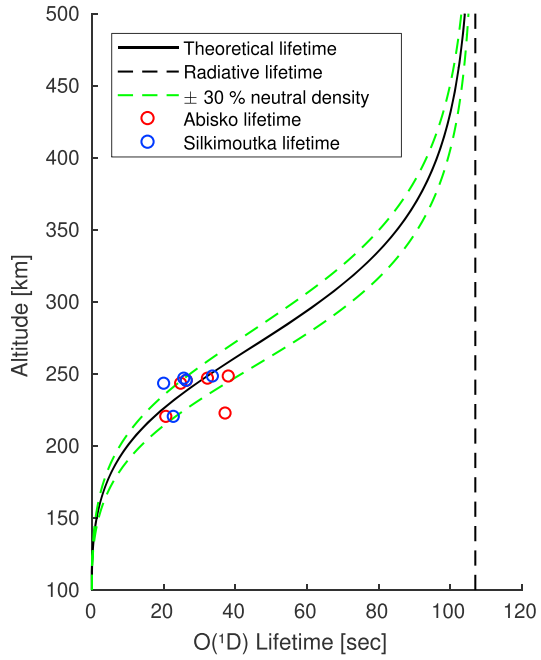

Figure 5. The figure depicts a comparison between the observed $O(^1D)$ lifetime and the theoretical $O(^1D)$ effective lifetime. Theoretical $O(^1D)$ effective lifetime estimates using ±30% of the MSIS-2000 neutral densities are included in the plot. The spread in observed $O(^1D)$ lifetime is large but agrees reasonably well with the theoretical $O(^1D)$ effective lifetime within the ±30 % neutral density confidence.

background reduction, and $\tilde{p}_s(i, j, I(\mathbf{V}_t))$ is the corresponding modeled image, the projection of the parametrized 3-D emission model, $I(\mathbf{V}_t)$, down to imaging station s. $[\mathbf{m_s} - \tilde{\mathbf{m}}_\mathbf{s}]$ is the image distance between the pixel value maxima in the observed and modeled images, marked with a black and a white dot in the observed images in Figure 4. W is a weight factor controlling the significance of the maxima coordinate difference.

To obtain accurate projections, both the field of view and the sensitivity of the cameras need to be known to high accuracy. Line-of-sight calibration was achieved by identifying stars in the image with the corresponding stars in the Yale Bright Star Catalog (Hoffleit & Jaschek,), the applied calibration method is described further in Gustavsson et al. (2008). Absolute intensity calibration factors from Wang (2011) were used to convert the Charge-Coupled Device counts to Rayleighs for images in 5,577 and in 6,300 Å. The Charge-Coupled Device sensitivity factors in the 8,446-Å emission line were determined by the irradiance spectra of the identified stars as given in the Pulkovo spectrometric catalog (Alekseeva et al., 1996).

3.2. Emission Model

The excitation-emission process was implemented in the aurora modeling in order to make the 3-D emission distributions comparable to the Gustavsson and Eliasson (2008) excitation profiles. The 5,577- and the 8,446-Å emission distributions were considered to be directly proportional to the excitation rate distributions. This is justified by the short radiative lifetime (0.7 s) of the $O(^1S)$ state and the spontaneous emission from the $O(3p^3P)$ state (Gustavsson et al., 2008). The effects of collisional de-excitation, quenching, can therefore be ignored. The effects of drift and diffusion are insignificant for $O(^1S)$ and negligible for $O(3p^3P)$, taking into account the short radiative lifetimes and that the size of the heated blob is about 20 km with drift speeds only up to a few hundred meters per second (Bernhardt et al., 2000; Gustavsson et al., 2001).

The $O(^1D)$ state has a radiative lifetime of 107 s. The $O(^1D)$-neutral collision frequency is higher than the $O(^1D)$ radiation frequency at lower F region altitudes. Most of the excited $O(^1D)$ states will therefore never emit 6,300-Å radiation before relaxation. Thus, the quenching needs to be accounted for in the I_{6300} 3-D aurora modeling. The quenching rate is predominantly dependent on the neutral density. The effective $O(^1D)$ lifetime can therefore be considered as a function of altitude. The $O(^1D)$ continuity model from Gustavsson and Eliasson (2008) was employed to calculate the altitude-dependent effective $O(^1D)$ lifetimes. Neutral temperatures and densities from the MSIS-2000 model (Picone et al., 2002) and electron temperatures and densities from the IRI model (Bilitza et al., 2014) were used in the effective $O(^1D)$ calculation. The resulting theoretical $O(^1D)$ lifetimes are presented in Figure 5 along with the observed $O(^1D)$ lifetimes from Abisko and Silkimuotka. The observed $O(^1D)$ lifetime is estimated from the 6,300-Å emission decay after heating offset.

Although the quenching considerably shortens the $O(^1D)$ lifetime, it is still relatively long, 30 s according to the theoretical estimate at a typical peak emission altitude of 245 km. Thus, the model function described in Gustavsson et al. (2001) was employed to account for the effects of the horizontal drift, diffusion, and the altitude-dependent intensity reduction from the quenching; see equations 3 and 7 in Gustavsson et al. (2001). The values of the $O(^1D)$ horizontal drift and diffusion are unknown; hence, the I_{6300} 3-D modeling requires three additional fitting parameters for all modeling methods: wind along the west-east direction, u_x, wind along the south-north direction, u_y, and diffusion, D. The vertical drift was neglected in the modeling, and it was assumed that the horizontal wind and the $O(^1D)$ diffusion were uniform within the heated volume.

4. Results

The best fit projections of the I_{6300} 3-D aurora models at 16.48.45 UT are presented in Figure 6 along with the comparison to the observed images at the matching time step. Note that an additional I_{6300} modified

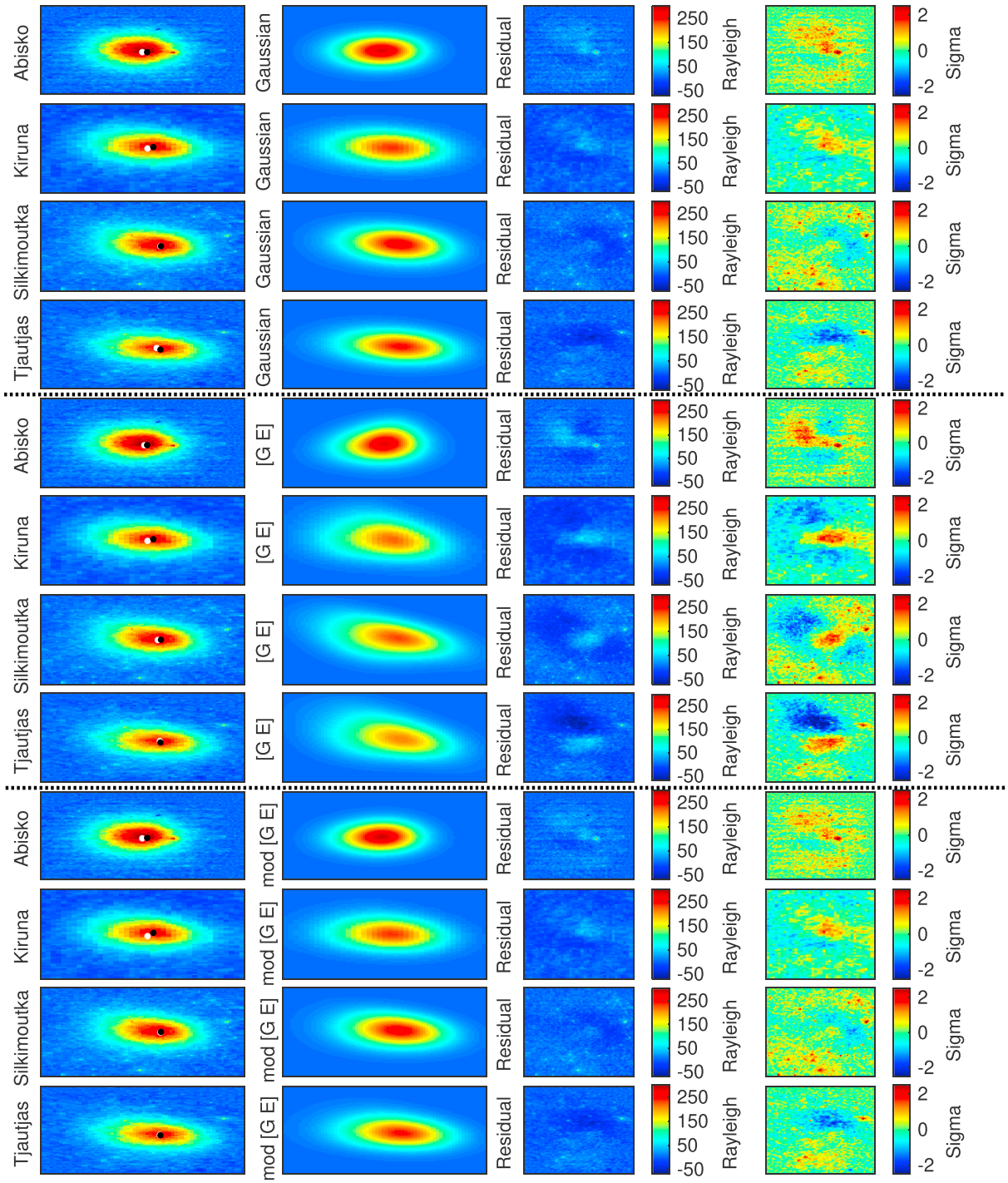

Figure 6. Rows 1-4 are the best fit Gaussian model projections, rows 5–8 are the best fit Gustavsson-Eliasson (G-E) model projections, and rows 9–12 are the best fit modified G-E model projections. The projections of the the Gaussian model and the modified G-E model are similar and in better agreement with the observed images than the projections of the G-E model. The pixel grids are similar to the pixel grids in Figure 4.

G-E model comparison, during 5.423-MHz heating, is presented in Figure 4. The remaining successful 3-D reconstruction results, 41 red aurora models, 15 green aurora models, and 2 infrared aurora models, for each of the three modeling methods, will not be presented in this article due to limited space.

Figure 6 clearly depicts a trend that is seen for all I_{6300} 3-D modeling results; the best fit projections of the the Gaussian and the modified G-E models are similar and in better agreement to the observed images

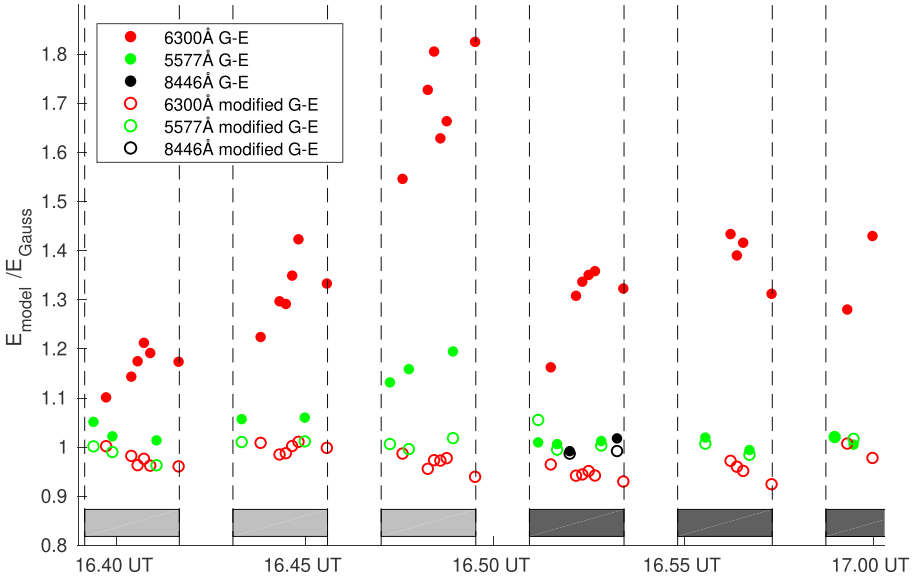

Figure 7. The Gustavsson-Eliasson (G-E) modeling produce I_{6300} projections with higher error values, E_{GE}, than both the Gaussian, E_{Gauss}, and the modified G-E, E_{modGE}, modeling methods, as seen by the error value ratios E_{GE}/E_{Gauss} and E_{modGE}/E_{Gauss}. The same trend is seen in the I_{5577} projections during 6.200-MHz pumping. As before, the light gray boxes represent heating on during 6.200-MHz pumping and the dark gray boxes heating on at 5.423-MHz pumping.

than the best fit G-E model projections. The same trend is also seen in the I_{5577} model projections during 6.200-MHz heating. There are, however, no significant deviation in the projections of the best fit models during 5.423-MHz pumping in I_{5577} and I_{8446}. The error values, from the error function in equation (1), of the best fit models were used to underline this result. Figure 7 presents the error value ratio between the G-E models and the Gaussian models, E_{GE}/E_{Gauss}, and the ratio between the modified *G-E* models and the Gaussian models E_{modGE}/E_{Gauss} at different time steps, t, and for all enhanced emissions. Figure 7 shows that the G-E modeling method produced model projections with less of an agreement to the observed images than the Gaussian model projections. On average, the G-E modeling produce I_{6300} projections with ~40% higher error values during 6.200- and 5.423-MHz heating and I_{5577} projections with ~10% higher error values during 6.200-MHz heating. The modified G-E modeling produce similar error values to the Gaussian modeling for all emission lines. It should be noted that the signal-to-noise ratio is much higher for I_{6300} than for I_{5577} and I_{8446}; see Rayleigh enhancement values in Figure 3. The discrepancy between the models might only be seen when the signal-to-noise ratio is high, which could explain why there are no clear deviations between the I_{5577} and I_{8446} model projections during 5.423-MHz pumping.

Mean excitation-altitude profiles were calculated to study the discrepancy between the physical G-E model and the empirical 3-D Gaussian and semiempirical modified G-E models. The resulting $O(^1D)$, $O(^1S)$, and $O(3p^3P)$ excitation-altitude profiles, for all modeling methods, are presented in Figure 8. Notice in Figure 8 that the Gaussian excitation rate profiles are in good agreement with the modified G-E excitation rate profiles for all excitation states and for both pump frequencies. Also note that Figure 8 only depicts the excitation rate distributions as a function of altitude. The deviations of the resulting 3-D aurora models will predominantly be along the altitude axis since all aurora models are created similarly in the horizontal plane, using a 2-D Gaussian distribution, but have different distribution functions along the magnetic field line. Normalized mean excitation-altitude profiles were used to produce the curves in Figure 8 in order to make the shape of excitation-altitude profiles comparable between all heating pulses. The normalized mean $O(^1D)$, $O(^1S)$, and $O(3p^3P)$ excitation rates in Figure 8 were calculated using 3-D reconstruction results during near steady state conditions in I_{6300}, I_{5577}, and I_{8446}, respectively. The 3-D reconstruction results from 16 I_{6300} models and 7 I_{5577} models during 6.200-MHz pumping and 7 I_{6300} models and 6 I_{5577} models during 5.423-MHz heating were used to produce the $O(^1D)$ and $O(^1S)$ excitation rate curves. Tomographic reconstruction in I_{8446} was successfully done at only two time steps. $O(3p^3P)$ excitation rate curves were therefore produced using two reconstruction results, both during 5.423-MHz pumping. The width of the curves in Figure 8 equals the $\pm\sigma$

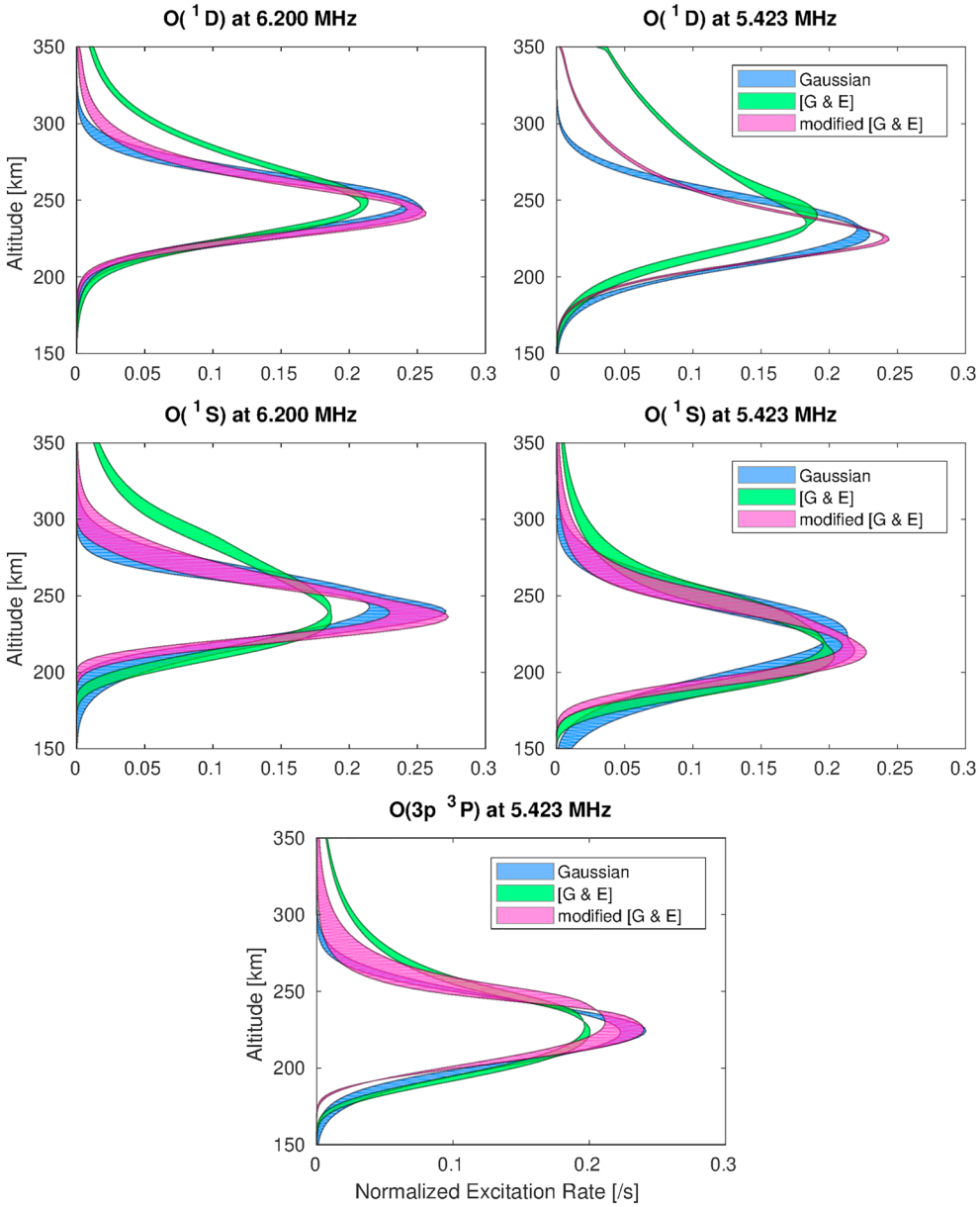

Figure 8. The figure depicts the resulting normalized mean excitation rates as a function of altitude for the three different 3-D aurora models; the empirical 3-D Gaussian model, the physical G-E model and hybrid modified G-E model. The best fit models from the the Gaussian and modified G-E methods have a smaller altitude range than predicted by the physical G-E model in $O(^1D)$ and $O(^1S)$ during 6.200-MHz pumping and in $O(^1D)$ during 5.423-MHz heating.

width for the $O(^1D)$ and $O(^1S)$ excitation rates. The edges of the $O(3p^3P)$ excitation rate curves are defined by the two resulting excitation profiles.

In addition, the best fit Gaussian model parameter values in altitude, z_0, horizontal width, σ_{xy}, and field-aligned width, σ_z, are presented in Figure 9 to depict the evolution of the $O(^1D)$, $O(^1S)$, and $O(3p^3P)$ volume excitation rates. The altitude of the excitation center drops from about 240 to 220 km when changing pump frequency from 6.200 to 5.423 MHz. This is a consequence of the electron density gradient in the lower F region. HF radio waves at a lower frequency will interact with a lower density plasma; the wave-plasma resonance altitude will therefore drop. The horizontal excitation width is about 12 km at 6.200-MHz heating and increases to around 16 km at 5.423-MHz heating. This increase is larger than the inferred ~1-km increase in the horizontal excitation width from the modeled beam patterns, as seen before in Figure 2.

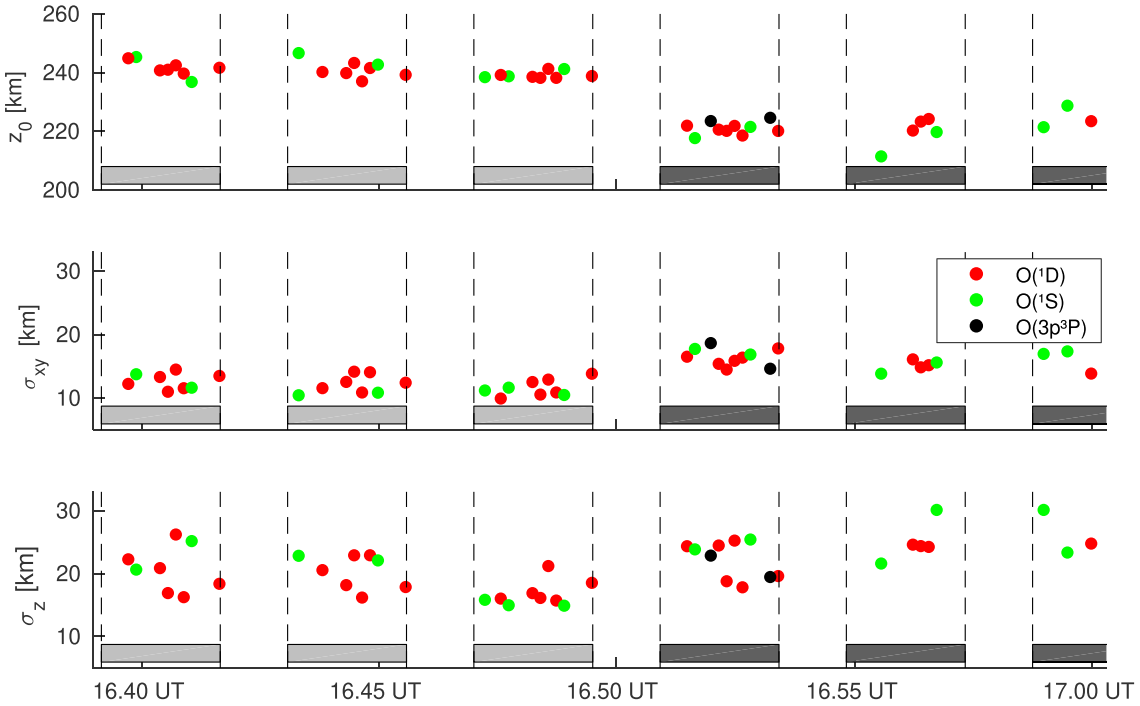

Figure 9. Gaussian best fit parameters, from top to bottom: Excitation center altitude, horizontal width, and width along the magnetic field. The light gray boxes represent heating on during 6.200-MHz pumping and the dark gray boxes heating on at 5.423-MHz pumping.

Additionally, in Figure 9, there is an apparent small increase in width along the magnetic field line when changing pumping frequency from 6.200 to 5.423 MHz, although the spread is somewhat large. There are no clear deviations in excitation center altitudes and widths between the different species.

5. Discussion

The main result in this article is that there are deviations between the physical G-E reconstructions and the empirical Gaussian and semiempirical modified G-E reconstructions. In particular, Figure 8 suggests that $O(^1D)$ and $O(^1S)$ excitation during 6.200-MHz heating and $O(^1D)$ excitation during 5.423-MHz pumping are induced within a smaller altitude range than predicted by Gustavsson and Eliasson (2008). This conclusion is based on three observations: (1) The model fits, an example is seen in Figure 6, are adequate to be meaningful fits. (2) The Gaussian and the modified G-E methods produce aurora models, which are significantly better than the best fit G-E model projections, as seen in Figure 7. (3) The excitation-altitude distributions of the G-E models are statistically inconsistent with the distributions of the Gaussian and the modified G-E models; see Figure 8.

An additional result is seen in Figure 3; I_{6300} and the electron temperature enhancement decreased when going from 6.200- to 5.423-MHz pumping, while the high threshold energy I_{8446} enhancement increased. Only a ~30% I_{6300} reduction can be explained by increased quenching at lower heating altitudes and about 15% electron temperature and I_{6300} reduction is caused by reduced power flux during 5.423-MHz pumping. A similar trend was reported in Gustavsson et al. (2006) by observing electron temperature enhancements, I_{6300}, I_{5577}, and the high threshold energy I_{4278} during a heating experiment with frequency stepping around the fourth gyroharmonic. Gustavsson et al. (2006) observed that I_{4278} was insignificant during heating far above or below the gyroharmonic and increased when heating a few tens of kilohertz above the fourth double resonance. This indicates, by comparison to Gustavsson et al. (2006), that heating occurred away from a gyroharmonic during 6.200-MHz pumping and just above the fourth gyroharmonic during 5.423-MHz pumping, although not close enough to the fourth double resonance to induce significant I_{4278}. The observations in Figure 3 and in Gustavsson et al. (2006) are in agreement with the Vlasov simulation results of accelerated electrons presented in Najmi et al. (2017). Najmi et al. (2017) argued that the electron energy distribution during heating just above the fourth gyroharmonic will have a more pronounced high-energy

tail than heating away from the gyroharmonic. The reason for this is that HF pumping just above the gyroharmonic will energize fewer electrons, but to higher energies through resonance acceleration by excited upper-hybrid waves. On the contrary, HF heating away from the gyroharmonic mainly enhances electron energization through bulk heating from electron Bernstein waves.

Three possible explanations to the confined excitation region, both during heating away and close to the fourth gyroharmonic, will be discussed: (1) anisotropic electron acceleration, (2) underestimated neutral densities, and (3) shortcomings in the Gustavsson and Eliasson (2008) electron transport model. Of these three, anisotropic electron acceleration appears to be the only viable explanation.

5.1. Anisotropic Electron Acceleration

The Gustavsson and Eliasson (2008) model assumes an isotropic electron acceleration, as assumed in other attempts to find the electron energy-altitude distribution during ionospheric F region heating at high latitudes (e.g., Gustavsson et al., 2005; Hysell et al., 2012, 2014). This assumption may, however, not be valid. Grach (1999) predicted that an anisotropic electron acceleration, with an enhanced population of energized electrons perpendicular to the magnetic field, would be induced when pumping in resonance with both the upper-hybrid frequency and an harmonic of the electron gyrofrequency; that is, $(f_h \simeq f_u \simeq nf_e)$ where n is an integer. Hence, the narrow excitation rate profiles during 5.423-MHz pumping could possibly be explained by double resonance heating in proximity to the fourth gyroharmonic frequency; that is, $(f_h \simeq f_u \simeq 4f_e)$. The deviation between the resulting excitation rate profiles at 6.200-MHz heating can, however, not be explained by proximity to the fourth double resonance point. Grach (1999) argued that the anisotropic component of the electron velocity distribution could be neglected during heating away from the double resonance due to isotropization of the accelerated electrons by scattering in the acceleration region.

The discrepancy between excitation rate profiles from the isotropic G-E modeling method and the excitation rate profiles from the empirical Gaussian and semiempirical modified G-E modeling can therefore only partly be related to the predictions of Grach (1999). Either the anisotropic component is more prominent than predicted during heating away from the double resonance or other mechanisms are responsible for the deviations between the predicted and empirically reconstructed excitation rate profiles.

5.2. Underestimated Neutral Density

The neutral densities from the MSIS-2000 model were used to calculate the Gustavsson and Eliasson (2008) profiles. An underestimation of the neutral densities would cause the Gustavsson and Eliasson (2008) profiles to miscalculate the electron-neutral collision frequency and favor a larger altitude range for the excitation. However, a crude underestimation of the neutral density would also cause a systematic difference between the theoretical and observed $O(^1D)$ lifetimes. No such difference is observed in Figure 5, and we therefore consider an underestimation of the neutral densities to be an unlikely cause for the discrepancy between the predicted and empirically reconstructed excitation rate profiles.

5.3. Shortcomings in the Gustavsson and Eliasson (2008) Transport Model

We cannot ignore the possibility of shortcomings in the two-stream electron transport model to be the cause of the deviations. However, none of the parameters in the Gustavsson and Eliasson (2008) transport model, apart from the neutral density, can cause significant altitude confinement of the excitation rates. In addition, the resulting electron energy distributions as a function of energy and altitude from Gustavsson and Eliasson (2008) are in apparent agreement with the results from Hysell et al. (2012, 2014), which employed a different electron transport model, the SAMI2-PE model (Varney et al., 2012). This indicates that the deviations between the predicted and empirically reconstructed excitation rate profiles do not likely originate from shortcomings or errors in the applied electron transport model.

6. Summary and Conclusions

In this paper, we have presented a method for comparing electron energy-altitude distributions to multiview point images by employing tomography-like inversion methods and excitation rate profiles, calculated using the method described in Gustavsson and Eliasson (2008). Modeling of the artificial aurora was done in the enhanced 6,300-, 5,577-, and 8,446-Å emission lines, providing estimates of the $O(^1D)$, $O(^1S)$, and $O(3p^3P)$ volume excitation rates. The resulting excitation rates, see Figure 8, indicate that the excitation rate distributions are less extended in altitude than predicted by the excitation rate profiles from Gustavsson and Eliasson (2008). The Gustavsson and Eliasson (2008) transport model assumes an isotropic electron accel-

eration. A possible explanation for this discrepancy might therefore be that HF heating both away from and just above the fourth double resonance induces an anisotropic distribution of energized electrons. Grach (1999) analytically predicted an anisotropic electron distribution, with an enhanced population perpendicular to the magnetic field, during HF heating near a double resonance point, but argued for isotropization of the accelerated electrons during HF pumping away from a double resonance point. A remaining open question is whether an anisotropic electron acceleration can lead to excitation rate profiles which are consistent with our observations. This conjecture could be investigated using a multistream electron transport model where all elastic and inelastic collisions are taken into account in addition to an anisotropic electron energization term. Additionally, the electron temperature enhancements and the emission enhancements during heating away and just above the fourth double resonance point are in agreement with the electron energy distributions obtained by Vlasov simulations of accelerated electrons, as presented in Najmi et al. (2017).

Appendix A: Aurora Models

A1. The Gaussian Model

The 3-D Gaussian aurora models are constructed using Gaussian distributions along all axes, $G(x, y, z, \sigma_{xy}, \sigma_z)$:

$$f(x,y,z) = I_0 \cdot \exp\left(-\left(\frac{X^2}{2\sigma_{xy}^2} + \frac{((Y + Z\sin(\theta))^2}{2\sigma_{xy}^2} + \frac{Z^2}{2\sigma_z^2}\right)\right) \tag{A1}$$

where

$$X, Y, Z = x - x_0, y - y_0, z - z_0 \tag{A2}$$

I_0 is the maximum excitation rate, located at the center of the excitation volume (x_0, y_0, z_0). The excitation distribution was assumed to have a symmetrical Gaussian shape in the horizontal plane; σ_{xy} is the horizontal $(1/e)$ width radius. θ is the magnetic field angle from zenith, 12°S at EISCAT Ramfjordmoen. σ_z is the width in altitude. The constructed excitation blob is allowed to be asymmetric ($\sigma_z \neq \sigma_{xy}$).

A2. The G-E and The Modified G-E Models

The G-E and the modified G-E modeling used excitation rate profiles, calculated using the method described in Gustavsson and Eliasson (2008), to construct the excitation-altitude distributions. $I_{z0}(z)$ is the normalized excitation rate profile as a function of altitude, z, with an excitation center at altitude z_0. A shape parameter, γ, was used to modify the shape of the normalized excitation-altitude profiles, $I_{z0}^{\gamma}(z)$. This yields the volume excitation function, $f(x, y, z)$:

$$f(x,y,z) = I_0 \cdot I_{z0}^{\gamma}(Z) \cdot \exp\left(-\left(\frac{X^2}{2\sigma_{xy}^2} + \frac{(Y + Z\sin(\theta))^2}{2\sigma_{xy}^2}\right)\right) \tag{A3}$$

The G-E modeling is defined by $\gamma = 1$; that is, the G-E excitation rate profiles were used directly. In the modified G-E modeling, the excitation rates were allowed to be modified by adjusting the γ value. A high gamma value ($\gamma > 1$) will sharpen the excitation rate profiles around the peak excitation altitude, z_0, whereas a low gamma value ($\gamma < 1$) will make the profiles more blunt.

A3. The Modeling Search Parameters

The required auroral modeling parameters, depending on the modeling method, are summarized in Table A1. The horizontal neutral wind and diffusion parameters are only necessary for the 6,300-Å

Table A1
The Search Parameters

Search parameter	Gaussian	G-E	Modified G-E
Maximum excitation	I_0	I_0	I_0
Excitation midpoint	x_0, y_0, z_0	x_0, y_0, z_0	x_0, y_0, z_0
Excitation radius/size	σ_{xy}, σ_z	σ_{xy}	σ_{xy}
Shape parameter			γ
(Neutral wind)	(u_x, u_y)	(u_x, u_y)	(u_x, u_y)
(Diffusion)	(D)	(D)	(D)
Number of parameters	6 (9)	5 (8)	6 (9)

emission modeling; these parameters are therefore within parenthesis. The vertical wind was assumed to be negligible.

Acknowledgments
ALIS is supported by the Swedish Research Council. EISCAT is an international association supported by research organizations in China (CRIRP), Finland (SA), Japan (NIPR and STEL), Norway (NFR), Sweden (VR), and the United Kingdom (NERC). A. Kvammen and J. Vierinen are supported by the Tromsø Research Foundation. The ALIS multistation images from the 16 February 2015 are available in the ALIS data archive (http://www.alis.irf.se/stdnames/2015/02/16/), and the EISCAT data are available in the Madrigal database. MatLab functions from the Auroral Image Data Analysis tools (AIDA-tools); http://www.alis.irf.se/~bjorn/AIDA_tools/, were used for camera calibration, data pre-processing and projection calculations from 3D volume emission rates to modeled image pixel intensities. The authors would like to thank the reviewers for valuable comments and suggestions.

References

Alekseeva, G., Arkharov, A., Galkin, V., Hagen-Thorn, E., Nikanorova, I., Novikov, V., et al. (1996). The Pulkovo spectrophotometric catalog of bright stars in the range from 320 to 1080 NM. *Baltic Astronomy*, *5*, 603–838.

Bernhardt, P. A., Siefring, C. L., Briczinski, S. J., McCarrick, M., & Michell, R. G. (2016). Large ionospheric disturbances produced by the HAARP HF facility. *Radio Science*, *51*, 1081–1093. https://doi.org/10.1002/2015RS005883

Bernhardt, P. A., Tepley, C. A., & Duncan, L. M. (1989). Airglow enhancements associated with plasma cavities formed during ionospheric heating experiments. *Journal of Geophysical Research*, *94*(A7), 9071–9092.

Bernhardt, P., Wong, M., Huba, J., Fejer, B. G., Wagner, L., Goldstein, J., et al. (2000). Optical remote sensing of the thermosphere with HF pumped artificial airglow. *Journal of Geophysical Research*, *105*(A5), 10,657–10,671.

Bilitza, D., Altadill, D., Zhang, Y., Mertens, C., Truhlik, V., Richards, P., et al. (2014). The International Reference Ionosphere 2012—A model of international collaboration. *Journal of Space Weather and Space Climate*, *4*(A07), 12.

Brändström, U. (2003). The Auroral Large Imaging System: Design, operation and scientific results.

Brändström, B. U. E., Leyser, T. B., Steen, Å., Rietveld, M. T., Gustavsson, B., Aso, T., & Ejiri, M. (1999). Unambiguous evidence of HF pump-enhanced airglow at auroral latitudes. *Geophysical Research Letters*, *26*(23), 3561–3564.

Carlson, H. C., Wickwar, V. B., & Mantas, G. P. (1982). Observations of fluxes of suprathermal electrons accelerated by HF excited instabilities. *Journal of Atmospheric and Terrestrial Physics*, *44*(12), 1089–1100.

Coster, A. J., Djuth, F. T., Jost, R. J., & Gordon, W. E. (1985). The temporal evolution of 3-m striations in the modified ionosphere. *Journal of Geophysical Research*, *90*(A3), 2807–2818.

Djuth, F. T., Isham, B., Rietveld, M. T., Hagfors, T., & La Hoz, C. (2004). First 100 ms of HF modification at Tromsø, Norway. *Journal of Geophysical Research*, *109*, A11307. https://doi.org/10.1029/2003JA010236

Djuth, F. T., Pedersen, T. R., Gerken, E. A., Bernhardt, P. A., Selcher, C. A., Bristow, W. A., & Kosch, M. J. (2005). Ionospheric modification at twice the electron cyclotron frequency. *Physical Review Letters*, *94*(12), 125001.

Eliasson, B., & Papadopoulos, K. (2015). Numerical study of anomalous absorption of O mode waves on magnetic field-aligned striations. *Geophysical Research Letters*, *42*, 2603–2611. https://doi.org/10.1002/2015GL063751

Gondarenko, N. A., Ossakow, S. L., & Milikh, G. M. (2005). Generation and evolution of density irregularities due to self-focusing in ionospheric modifications. *Journal of Geophysical Research*, *110*, A09304. https://doi.org/10.1029/2005JA011142

Grach, S. M. (1999). On kinetic effects in the ionospheric F-region modified by powerful radio waves. *Radiophysics and Quantum Electronics*, *42*(7), 572–588.

Grach, S., Sergeev, E., Mishin, E., & Shindin, A. V. (2017). Dynamic properties of ionospheric plasma turbulence driven by high-power high-frequency radiowaves. *Physics-Uspekhi*, *59*(11), 1091.

Gurevich, A. V. (2007). Nonlinear effects in the ionosphere. *Physics-Uspekhi*, *50*(11), 1091–1121.

Gurevich, A. V., & Zybin, K. P. (2006). Strong field aligned scattering of UHF radio waves in ionospheric modification. *Physics Letters A*, *358*(2), 159–165.

Gustavsson, B., Brändström, B. U. E., Steen, Å., Sergienko, T., Leyser, T. B., Rietveld, M. T., et al. (2002). Nearly simultaneous images of HF-pump enhanced airglow at 6300 Åand 5577 Å. *Geophysical Research Letters*, *29*(24), 2220. https://doi.org/10.1029/2002GL015350

Gustavsson, B., & Eliasson, B. (2008). Hf radio wave acceleration of ionospheric electrons: Analysis of HF-induced optical enhancements. *Journal of Geophysical Research*, *113*, A08319. https://doi.org/10.1029/2007JA012913

Gustavsson, B. J., Kosch, M., Wong, A., Pedersen, T., Heinselman, C., Mutiso, C., et al. (2008). First estimates of volume distribution of HF-pump enhanced emissions at 6300 and 5577 å: A comparison between observations and theory.

Gustavsson, B., Leyser, T. B., Kosch, M., Rietveld, M. T., Steen, Å., Brändström, B. U. E., & Aso, T. (2006). Electron gyroharmonic effects in ionization and electron acceleration during high-frequency pumping in the ionosphere. *Physical Review Letters*, *97*(19), 195002.

Gustavsson, B., Sergienko, T., Kosch, M., Rietveld, M., Brändström, B., Leyser, T., et al. (2005). The electron energy distribution during HF pumping, a picture painted with all colors. *In Annales Geophysicae*, *23*, 1747–1754.

Gustavsson, B., Sergienko, T., Rietveld, M. T., Honary, F., Steen, A., Brändström, B. U. E., et al. (2001). First tomographic estimate of volume distribution of HF-pump enhanced airglow emission. *Journal of Geophysical Research*, *106*(A12), 29,105–29,123.

Haslett, J. C., & Megill, L. R. (1974). A model of the enhanced airglow excited by RF radiation. *Radio Science*, *9*(11), 1005–1019.

Hoffleit, D., & Jaschek, C.The bright star catalogue. New Haven, Conn.: Yale University Observatory, c1991, 5th rev. ed., edited by Hoffleit, Dorrit; Jaschek, Carlos.

Holma, H., Kaila, K. U., Kosch, M. J., & Rietveld, M. T. (2006). Recognizing the blue emission in artificial aurora. *Advances in Space Research*, *38*(11), 2653–2658.

Honary, F., Stocker, A., Robinson, T., Jones, T., & Stubbe, P. (1995). Ionospheric plasma response to HF radio waves operating at frequencies close to the third harmonic of the electron gyrofrequency. *Journal of Geophysical Research*, *100*(A11), 21,489–21,501.

Hysell, D. L., Miceli, R. J., Kendall, E. A., Schlatter, N. M., Varney, R. H., Watkins, B. J., et al. (2014). Heater-induced ionization inferred from spectrometric airglow measurements. *Journal of Geophysical Research: Space Physics*, *119*, 2038–2045. https://doi.org/10.1002/2013JA019663

Hysell, D. L., Varney, R. H., Vlasov, M. N., Nossa, E., Watkins, B., Pedersen, T., & Huba, J. D. (2012). Estimating the electron energy distribution during ionospheric modification from spectrographic airglow measurements. *Journal of Geophysical Research*, *117*, A02317. https://doi.org/10.1029/2011JA017187

Istomin, Y. N., & Leyser, T. (2003). Electron acceleration by cylindrical upper hybrid oscillations trapped in density irregularities in the ionosphere. *Physics of Plasmas*, *10*(7), 2962–2970.

Kendall, E., Marshall, R., Parris, R. T., Bhatt, A., Coster, A., Pedersen, T., et al. (2010). Decameter structure in heater-induced airglow at the High frequency Active Auroral Research Program facility. *Journal of Geophysical Research*, *115*, A08306. https://doi.org/10.1029/2009JA015043

Kosch, M. J., Rietveld, M. T., Kavanagh, A. J., Davis, C., Yeoman, T. K., Honary, F., & Hagfors, T. (2002). High-latitude pump-induced optical emissions for frequencies close to the third electron gyro-harmonic. *Geophysical Research Letters*, *29*(23), 2112. https://doi.org/10.1029/2002GL015744

Lagarias, J. C., Reeds, J. A., Wright, M. H., & Wright, P. E. (1998). Convergence properties of the Nelder–Mead simplex method in low dimensions. *SIAM Journal on Optimization*, *9*(1), 112–147.

Lehtinen, M. S., & Huuskonen, A. (1996). General incoherent scatter analysis and GUISDAP. *Journal of Atmospheric and Terrestrial Physics*, *58*(1), 435–452.

Leyser, T. B. (2001). Stimulated electromagnetic emissions by high-frequency electromagnetic pumping of the ionospheric plasma. *Space Science Reviews*, *98*(3-4), 223–328.

Mantas, G. P. (1994). Large 6300-Åairglow intensity enhancements observed in ionosphere heating experiments are excited by thermal electrons. *Journal of Geophysical Research*, *99*(A5), 8993–9002.

Mantas, G. P., & Carlson, H. C. (1996). Reinterpretation of the 6300-Åairglow enhancements observed in ionosphere heating experiments based on analysis of Platteville, Colorado, data. *Journal of Geophysical Research*, *101*(A1), 195–209.

Milikh, G., Gurevich, A., Zybin, K., & Secan, J. (2008). Perturbations of GPS signals by the ionospheric irregularities generated due to HF-heating at triple of electron gyrofrequency. *Geophysical Research Letters*, *35*, L22102. https://doi.org/10.1029/2008GL035527

Najmi, A., Eliasson, B., Shao, X., Milikh, G., Sharma, A. S., & Papadopoulos, K. (2017). Vlasov simulations of electron acceleration by radio frequency heating near the upper hybrid layer. *Physics of Plasmas*, *24*(10), 102904.

Pedersen, T., Gustavsson, B., Mishin, E., MacKenzie, E., Carlson, H., Starks, M., & Mills, T. (2009). Optical ring formation and ionization production in high-power heating experiments at HAARP. *Geophysical Research Letters*, *36*, L18107. https://doi.org/10.1029/2009GL040047

Picone, J. M., Hedin, A. E., Drob, D. P., & Aikin, A. C. (2002). NRLMSISE-00 empirical model of the atmosphere: Statistical comparisons and scientific issues. *Journal of Geophysical Research*, *107*(A12), 1468.

Rietveld, M. T., Kohl, H., Kopka, H., & Stubbe, P. (1993). Introduction to ionospheric heating at Tromsø I. Experimental overview. *Journal of atmospheric and terrestrial physics*, *55*(4-5), 577–599.

Rietveld, M. T., Kosch, M. J., Blagoveshchenskaya, N. F., Kornienko, V. A., Leyser, T. B., & Yeoman, T. K. (2003). Ionospheric electron heating, optical emissions, and striations induced by powerful HF radio waves at high latitudes: Aspect angle dependence. *Journal of Geophysical Research*, *108*(A4), 1141. https://doi.org/10.1029/2002JA009543

Rietveld, M. T., Senior, A., Markkanen, J., & Westman, A. (2016). New capabilities of the upgraded EISCAT high-power HF facility. *Radio Science*, *51*, 1533–1546. https://doi.org/10.1002/2016RS006093

Rishbeth, H., & Van Eyken, A. (1993). EISCAT: Early history and the first ten years of operation. *Journal of atmospheric and terrestrial physics*, *55*(4-5), 525–542.

Robinson, T. (1989). The heating of the high lattitude ionosphere by high power radio waves. *Physics reports*, *179*(2-3), 79–209.

Rydesäter, P., & Gustavsson, B. (2000). Investigation of smooth basis functions and an approximated projection algorithm for faster tomography. *International journal of imaging systems and technology*, *11*(6), 347–354.

Senior, A., Rietveld, M. T., Yeoman, T. K., & Kosch, M. J. (2012). The dependence of F-region electron heating on HF radio pump power: Measurements at EISCAT Tromsø. *Journal of Geophysical Research*, *117*, A04309. https://doi.org/10.1029/2011JA017267

Shindin, A., Klimenko, V., Kogogin, D., Beletsky, A., Grach, S., Nasyrov, I., & Sergeev, E. (2018). Spatial characteristics of the 630-nm artificial ionospheric airglow generation region during the Sura facility pumping. *Radiophysics and Quantum Electronics*, *60*(11), 849–865.

Stubbe, P., Stocker, A. J., Honary, F., Robinson, T. R., & Jones, T. B. (1994). Stimulated electromagnetic emissions and anomalous HF wave absorption near electron gyroharmonics. *Journal of Geophysical Research*, *99*(A4), 6233–6246.

Varney, R. H., Swartz, W. E., Hysell, D. L., & Huba, J. D. (2012). SAMI2-PE: A model of the ionosphere including multistream interhemispheric photoelectron transport. *Journal of Geophysical Research*, *117*, A06322. https://doi.org/10.1029/2011JA017280

Wang, Z. (2011). Absolute calibration of ALIS cameras.